



Cite this: *Phys. Chem. Chem. Phys.*,
2024, 26, 14908

Received 3rd January 2024,
Accepted 30th April 2024

DOI: 10.1039/d4cp00020j

rsc.li/pccp

A high-performance electrocatalyst *via* graphitic carbon nitride nanosheet-decorated bimetallic phosphide for alkaline water electrolysis†

Zehra Kayış  and Duygu Akyüz *

Developing renewable and clean energy systems for overall water electrolysis requires low-cost, highly efficient, and stable catalysts. With this motivation, nickel cobalt phosphorus (NiCoP) was electro-deposited onto nickel foam (NF) and then modified with graphitic carbon nitride (g-C₃N₄). The designed g-C₃N₄/NiCoP/NF electrode was used for the hydrogen evolution reaction (HER) and oxygen evolution reaction (OER) in alkaline water electrolysis. It exhibited a small overpotential of 80 mV@10 mA cm^{−2} with a Tafel slope of 89 mV dec^{−1} for the HER. It also exhibited an overpotential of 370 mV@10 mA cm^{−2} with a Tafel slope of 64 mV dec^{−1} for the OER. The g-C₃N₄/NiCoP catalyst exhibited satisfactory stability in an alkaline electrolyzer system, in which g-C₃N₄/NiCoP/NF was used as the anode and cathode. Meanwhile, the electrocatalyst requires only a cell voltage of 1.70 V to achieve 10 mA cm^{−2} current density for overall water electrolysis.

1. Introduction

The worldwide energy crisis has led researchers to seek alternative energy sources other than fossil fuels. Among alternative energies, hydrogen can be accepted as the energy of the future.^{1,2} Some of the advantages are clean energy, high energy density and energy conversion efficiencies, different ways of storage, and energy carriers.³ In sustainable hydrogen gas (H₂) production, electrochemical and photochemical water splitting can play an important role in tackling global energy crises in an environmentally friendly way.⁴ Overall, water electrolysis occurs with two half-reactions including the hydrogen evolution reaction (HER) and the oxygen evolution reaction (OER). Under standard conditions, the real potential of water electrolysis is much higher than its thermodynamic potential (1.23 V). It is well known that platinum (Pt) is the most effective HER electrocatalyst.^{5,6} However, its high cost and low reserves greatly limit its commercial application.⁷ Therefore, catalyst development using non-noble metal alternatives to Pt is required for high stability, low overpotential, and high catalytic activity. Moreover, Pt oxides do not serve well for the OER as they cause the conductivity to decrease. Other precious metals such as Ir, Rh, Ru and their metal alloys are used as catalysts in the OER.⁸ Although the decomposition of water was first

carried out in an acidic medium, electrolysis of water in alkaline media has been studied for industrial applications for centuries.⁹ Alkaline water electrolysis has some disadvantages, such as low current density owing to the increased ohmic loss¹⁰ and small active electrode surface area. Researchers have developed an anion-exchange membrane (AEM) technology to overcome these limitations.¹¹ It is anticipated that the AEM will provide technical and cost advantages in more advanced and large-scale hydrogen production in the future compared to traditional alkaline electrolysis technology.¹¹

Recently, many electrocatalysts such as transition metal-based alloys,¹² sulfides,¹³ phosphides,¹⁴ carbides¹⁵ and selenides¹⁶ have been developed for the HER in alkaline media. Among the electrocatalysts, transition metal phosphides (TMPs) are popular as effective electrocatalysts for water electrolysis.^{17–19} Moreover, TMPs have advantages such as a tunable electronic structure, low price, and high durability over a wide pH range. For example, CoP-based materials have unique physical properties, such as superior charge transfer, owing to their P-rich components.²⁰ Acting as a proton acceptor, P can promote the formation of metal hydrides, thereby accelerating hydrogen production by electrochemical desorption. Recent studies have suggested that a second metal can be added to phosphite to improve catalytic performance.^{21–23} Lian *et al.*²⁴ synthesized Co–Fe bimetal phosphides using a precipitation method and achieved an overpotential of 133 mV@10 mA cm^{−2} in 1.0 M KOH. Liang *et al.* synthesized NiCoP on Ni foam using a plasma-assisted approach. The catalyst exhibited a HER overpotential of 32 mV@10 mA cm^{−2} current density in alkaline media.²⁵ In another study, NiCoP nanopeapods

Department of Chemistry, Faculty of Science, Gebze Technical University, Kocaeli, Turkey. E-mail: dakyuz@gtu.edu.tr

† Electronic supplementary information (ESI) available. See DOI: <https://doi.org/10.1039/d4cp00020j>



(the morphological structures of carbon nanotubes and NiCoP's resemblance to pae and pods, respectively; therefore, they are called NiCoP nanopeapods) were synthesized by a three-step hydrothermal-carbonization-phosphorization process. They reported a decrease in the overpotential of up to 82 mV@ 10 mA cm⁻² with a NiCoP nanopeapod/CNT electrode.²⁶ Although good performance of HER electrodes has been achieved in previous studies, the synthesis processes are complex and time-consuming.

2D materials such as graphene oxide, graphene, graphite carbon nitride (g-C₃N₄), metal chalcogenides, and transition metal carbide, nitride or carbonitrides (MXene) have recently attracted considerable attention owing to their unique properties.^{27–30} Among various 2D materials, g-C₃N₄ has a layered structure that can be considered as an *N*-substituted graphite framework consisting of π -conjugated graphite planes due to the presence of sp² hybridization of C and N atoms.³¹ g-C₃N₄ has high stability, an easy synthesis route, abundance, wide surface area, and tunable electronic structures.^{32–34} In addition, g-C₃N₄ also has properties such as being insoluble in acidic, alkaline, and organic solvents and having high thermal stability.³⁵ Despite these important advantages, the use of g-C₃N₄ alone is insufficient because of its poor water dissociation ability.³²

In this study, we carried out the synthesis of NiCoP by electrodeposition, which is an easy and fast synthesis method. Potentiostatic electrodeposition was applied in one step to fabricate films of Ni and Co phosphides on nickel foam (NF). To increase the electrocatalytic activity of NiCoP, the electrode was modified with graphitic carbon nitride. g-C₃N₄ was synthesized by the thermal treatment of urea and deposited on NiCoP/NF by a drop-dry process. To the best of our knowledge, the electrocatalyst obtained as a result of NiCoP electrodeposition on NF and its modification with g-C₃N₄ for use in alkaline water electrolysis has not yet been reported. The electrochemical activity of the NiCoP catalyst was increased by changing the Ni to Co ion ratio. The obtained electrode (g-C₃N₄/NiCoP/NF) was used as both the anode and cathode in the overall water electrolysis (OWE) in alkaline electrolytes.

2. Experimental

2.1 Chemicals

For the synthesis of g-C₃N₄ and NiCoP, urea (ISOLAB), nickel(II) chloride hexahydrate (NiCl₂·6H₂O) (Sigma Aldrich), cobalt(II) chloride hexahydrate (CoCl₂·6H₂O) (Sigma Aldrich), sodium hypophosphite monohydrate (NaH₂PO₂) (ZAG Kimya), ammonium chloride (NH₄Cl) (Emsure) and nitric acid (Emsure) were purchased. Pt/C (5%) (Sigma Aldrich) and ruthenium(IV) oxide (RuO₂) (Sigma Aldrich) were used as reference electrocatalysts for the HER and OER, respectively. Potassium hydroxide (KOH) (Merck), HCl (Merck), ethanol (Merck) and acetone (Merck) were purchased and used without purification. Pure water (≥ 18 M, Millipore) was used to clean the NF and to prepare electrolytes.

2.2 Characterization

The surface characterization of the materials was carried out by scanning electron microscopy (SEM; FEI-Nova). X-ray photoelectron spectroscopy (XPS) was performed using a monochromatized Al K alpha excitation source (Thermo Scientific K-Alpha model). X-ray diffraction (XRD) analysis was performed using an X-ray device (Model: BRUKER D-8 ADVANCE). Fourier transform infrared (FT-IR) analyses were performed using a JPEFT-IR PerkinElmer 100 instrument.

2.3 Electrochemical characterization

Linear sweep voltammetry (LSV), electrochemical impedance spectroscopy (EIS) and chronoamperometry (CA) were run in a three-electrode system using a Gamry 1010B potentiostat. The three-electrode configuration was created with an NF (working, 0.5 × 0.5 cm², thickness: 1.6 mm), a platinum plate (counter), and mercury/mercury oxide (Hg/HgO) (reference) in the luggin capillary. The data recorded according to the Hg/HgO were adjusted to a reversible hydrogen electrode (RHE) using the equation $E_{\text{RHE}} = E_{\text{Hg/HgO}} + 0.098 + 0.0591 \times \text{pH}$. All the electrochemical analyses were conducted in 8 mL of 1.0 M KOH. NF electrodes were cleaned in 6.0 M HCl, ethanol, acetone, and ultra-pure water by ultrasonication for 5 min. LSV studies were conducted at a 2 mV s⁻¹ scan rate at a potential between 0.3 V and -0.3 V for the HER and 1.0 V and 1.65 V for the OER *versus* RHE. The logarithmic values of the current density (from the LSV data) *versus* the overpotential values were plotted in the Tafel graph. Subsequently, a linear fit was applied to the Tafel region, and the Tafel slopes were calculated. EIS measurements were conducted in the frequency range of 0.1 Hz to 10 kHz with an AC amplitude of 10 mV. EIS data were fitted by using the Gamry Echem Analyst program. For the stability test, repetitive LSVs were performed at 100 mV s⁻¹ over 1000 cycles.

2.4 Synthesis of g-C₃N₄

The synthesis procedure of Liu *et al.*³⁶ was used for g-C₃N₄. Briefly, 10 g of urea was placed in a covered crucible in a muffle furnace (Protherm). Urea was heated to 550 °C for 3 hours under an air atmosphere. Then, the product (yellow color) was cleaned with 0.1 M nitric acid and then with distilled water three times. The obtained bulk material was dried at 80 °C for 24 h in a furnace.

Subsequently, g-C₃N₄ (5 mg) in 5 μ L of Nafion and DMF (0.5 mL) was dispersed by ultrasonication for 30 minutes. 50 μ L of the solution was deposited on the NF. The electrode was then dried on a hotplate at 80 °C. The drop-drying process was repeated 1, 2, and 3 times to determine the effect of the amount of g-C₃N₄ catalyst on the overpotential. A similar process was used to prepare RuO₂/NF and Pt/C/NF electrodes.

2.5 Synthesis of NiCoP

NiCoP was synthesized by the one-step electrodeposition on the NF.³⁷ First, 2 mM NiCl₂·6H₂O, 2 mM CoCl₂·6H₂O, 5 mM NH₄Cl, and 5 mM NaH₂PO₂ were mixed with 50 mL of distilled water. The solution was transferred to a three-electrode cell.



Electrodeposition was carried out at a deposition potential of -1.0 V vs. Hg/HgO and electrodeposition times of 50, 100, 200, 300 and 400 s using CA. For comparison, NiCoP catalysts with different Ni:Co weight ratios were prepared and are represented as NiCoP(0:1), NiCoP(1:0), NiCoP(1:1), NiCoP(3:1) and NiCoP(1:3).

2.6 Preparation of the g-C₃N₄/NiCoP/NF electrode

An optimized amount of g-C₃N₄ catalyst was dropped on the NiCoP/NF electrode and dried under vacuum at room temperature. The prepared g-C₃N₄/NiCoP/NF electrode was used as the working electrode in a three-electrode configuration in an alkaline electrolyte. The g-C₃N₄/NiCoP/NF electrode also served as both the anode and cathode for overall alkaline water electrolysis in an H-type electrolyzer.

2.7 Measurement of overall water electrolysis

The prepared g-C₃N₄/NiCoP/NF (0.5×0.5 cm²) served as an anode and cathode in an H-type electrolyzer. An N-117 proton exchange membrane was used in the H-cell. Electrolysis was carried out in 1.0 M KOH.

3. Results and discussion

3.1 Optimization of conditions

The standard reduction potentials of $E_{\text{Co}_2^{+}/\text{Co}}^0$ and $E_{\text{Ni}_2^{+}/\text{Ni}}^0$ at 298 K are -0.28 V and -0.23 V vs. SHE. The closeness of standard reduction potentials of Ni and Co allows co-deposition. It is known theoretically that P cannot be deposited alone in aqueous solutions but can be deposited in the presence of iron group elements (Fe, Ni Co).³⁸ Anuratha *et al.* reported that the cathodic reduction peak of metal phosphide (Co-P, Ni-P or Ni-Co-P) was around -0.7 V vs. Ag/AgCl and that there were small differences in the peak current densities.³⁸ Different electrodeposition potential values (in the range from 0.7 V to -1.2 V) were tried at CA. It was optimized at -1.0 V. To determine the optimal conditions of

the catalysts, the effects of experimental parameters such as the thickness of the catalyst, the ratio of Ni:Co, the electrodeposition time of NiCoP, and the amount of g-C₃N₄ were tested. These parameters were determined by recording the LSV in 1.0 M KOH. First, NiCoP was electrodeposited on the NF electrode using CA at a constant voltage of -1.0 V for 200 s to optimize the Ni:Co ratio. Then, LSV for the OER was applied in the potential range of 1.0 V and 2.1 V (vs. RHE), as shown in Fig. S1a (ESI†). Among the NiCoP(0:1), NiCoP(1:0), NiCoP(1:1), NiCoP(3:1), and NiCoP(1:3) catalysts, NiCoP(1:1) exhibited the highest current density and lowest onset potential. Moreover, the bar graph derived from LSV clearly shows that the Ni:Co ratio of 1:1 indicates the lowest overpotential compared to others for the OER (Fig. S1b, ESI†). The thickness of NiCoP was optimized by changing the electrodeposition times to 50, 100, 200, 300, and 400 s, and then, LSV was applied to the prepared electrode, and bar graphs were obtained (Fig. S1c, ESI†). The NiCoP/NF film reached a minimum overpotential value at an electrodeposition time of 100 s and then increased with further electrodeposition time. Fig. S1d (ESI†) shows a bar graph of overpotential at 50 mA cm⁻² versus the thickness of g-C₃N₄ on the NF. g-C₃N₄ on the NF was deposited according to the drop-dry process, and the lowest overpotential value was recorded for the prepared electrode with 100 μ L of g-C₃N₄. Finally, g-C₃N₄ (100 μ L)/NiCoP (Ni:Co, 1:1) (electrodeposition time: 100 s)/NF electrode was used for the HER, OER, and OWE in alkaline electrolytes.

3.2 Evaluation of structural and morphological analyses of the catalysts

FT-IR and XRD analysis were employed to confirm the successful synthesis of g-C₃N₄ and g-C₃N₄/NiCoP catalysts. The FT-IR spectrum of g-C₃N₄ (Fig. 1a) exhibited vibration peaks at 806.8, 1230.5, 1313.0, 1399.2, 1460.3, 1546.0, 1625.8, 1625.8, 1546.0, 1460.3, 1399.2, 1313.0, 1230.5, 1459.2, 1403.7, 1315.0, 1243.1, 1139.6, 813.2, 1631.5, 1849.0, 1562.9, 2090.7, 2340.2, 2767.4, 2888.4, 3160.6, 3178.8 cm⁻¹, which can be attributed to the bending vibration of the tri-s-triazine ring and stretching vibration of C-N and C=N, respectively.³⁹ The bands at 1313.0 and 1230.5 cm⁻¹ corresponded to the stretching vibration of the C-N(-C)-C or C-NH-C connected units.³⁶ The wide band at

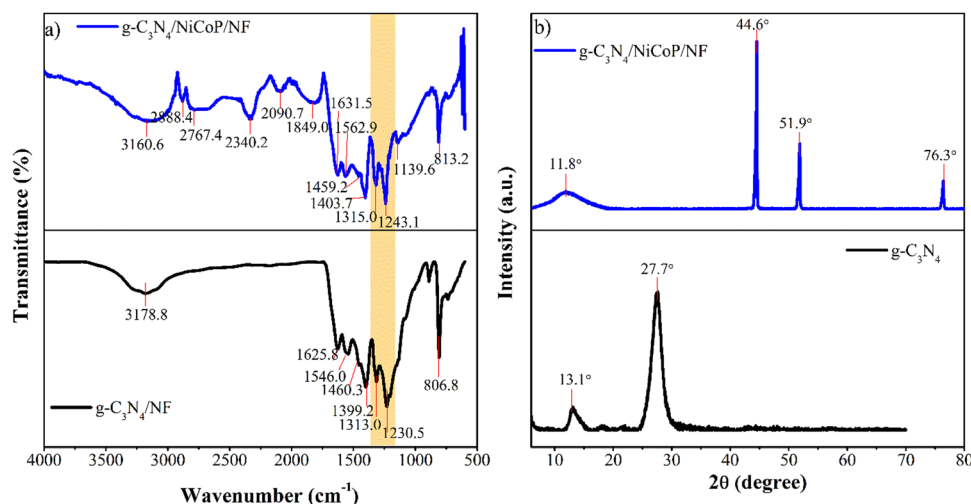


Fig. 1 (a) FT-IR and (b) XRD analyses of g-C₃N₄/NF and g-C₃N₄/NiCoP/NF electrodes.



3178.8 cm^{-1} is attributed to the stretching modes of NH .⁴⁰ In addition, there were no significant differences between the $\text{g-C}_3\text{N}_4$ and $\text{g-C}_3\text{N}_4/\text{NiCoP}$ spectra, suggesting that the $\text{g-C}_3\text{N}_4/\text{NiCoP}$ catalyst maintained its chemical structure, similar to that of $\text{g-C}_3\text{N}_4$. The FT-IR spectra were compatible with those reported in the literature.⁴¹

Crystallographic analyses were performed to determine the crystalline phases of the $\text{g-C}_3\text{N}_4/\text{NiCoP}$ catalysts. The XRD patterns of $\text{g-C}_3\text{N}_4$ and $\text{g-C}_3\text{N}_4/\text{NiCoP}/\text{NF}$ are shown in Fig. 1b. Ni foam shows three diffraction peaks at $2\theta = 44.5^\circ$, 52.0° and 76.5° , corresponding to the (1 1 1), (2 0 0) and (2 2 0) lattice planes, respectively.^{42,43} The XRD peaks of $\text{g-C}_3\text{N}_4$ centered at 27.7° and 13.1° are related to the interlayer stacking of aromatic ring segments and repeating units of tri-s-triazine, respectively.^{41,44} The diffraction peaks of $\text{g-C}_3\text{N}_4/\text{NiCoP}/\text{NF}$ were located at $2\theta = 11.8^\circ$, 44.6° , 51.9° and 76.3° . Moreover, no additional diffraction peaks were observed, except for the peak originating from $\text{g-C}_3\text{N}_4$, which suggests the presence of NiCoP.

The valence states and elemental compositions of NiCoP/NF and $\text{g-C}_3\text{N}_4/\text{NiCoP}/\text{NF}$ electrodes were determined by XPS. Fig. 2a shows the XPS survey spectrum, which confirms the presence of Ni, Co, and P. In addition, N originating from $\text{g-C}_3\text{N}_4$ was seen at 409.6 eV. Fig. 2b presents the high-resolution C 1s spectrum of the $\text{g-C}_3\text{N}_4/\text{NiCoP}/\text{NF}$ electrode. As depicted in Fig. 2b, the C1s peak is observed at 284.91 and 287.39 eV, which can be attributed to the typical C-C bond and the N-C=N bonds in the tri-s-triazine ring of $\text{g-C}_3\text{N}_4$.⁴⁵ Fig. 2c depicts the high-resolution O 1s spectra, where the NiCoP/NF and $\text{g-C}_3\text{N}_4/\text{NiCoP}/\text{NF}$ electrodes show one peak at 531.44 and 531.77 eV,

respectively, related to the P-O bond due to adsorption of NaH_2PO_2 .⁴³ Fig. 2d exhibits the presence of two peaks at around 874.20 and 856.40 eV, assigned to $\text{Ni } 2p_{1/2}$ and $\text{Ni } 2p_{3/2}$, respectively, with two satellite (sat.) peaks stemming from the presence of Ni(II) .⁴⁶ The high-resolution Co 2p shows two peaks at 797.55 eV belonging to $\text{Co } 2p_{1/2}$ and 781.65 eV belonging to $\text{Co } 2p_{3/2}$, which can be related to the Co-P bond stemming from transition metal phosphides, and its satellite can be attributed to oxidized Co(II) (Fig. 2e).⁴⁷ The high-resolution P 2p indicates one peak at 133.15 eV, which can be associated with the phosphate species (P-O) (Fig. 2f).⁴⁸ According to the above results, the comparison of $\text{g-C}_3\text{N}_4/\text{NiCoP}$ and NiCoP showed small positive and negative shifts in the bond energies of C 1s, O 1s, Ni 2p, Co 2p, and P 2p. This suggests that the addition of $\text{g-C}_3\text{N}_4$ increases the electron interactions between the elements. The detailed XPS fitting results of $\text{g-C}_3\text{N}_4/\text{NiCoP}$ and NiCoP are listed in Table S2 (ESI†). The peak intensities of C 1s, O 1s, Ni 2p and Co 2p for $\text{g-C}_3\text{N}_4/\text{NiCoP}/\text{NF}$ were higher than those of NiCoP/NF, which demonstrates strong electron interactions after $\text{g-C}_3\text{N}_4$. Interestingly, the peak intensity decreases for P 2p, which may be responsible for the charge transfer of $\text{g-C}_3\text{N}_4$ from Ni and Co to P, as P may have a lower partial negative charge.⁴⁹

The surface morphologies of the $\text{g-C}_3\text{N}_4/\text{NF}$ and $\text{g-C}_3\text{N}_4/\text{NiCoP}/\text{NF}$ electrodes were investigated by SEM at different magnifications ($250\times$ and $5000\times$), as shown in Fig. 3. The SEM images of $\text{g-C}_3\text{N}_4$ show a nanosheet-type morphology (Fig. 3a and b). The high-magnification SEM images of $\text{g-C}_3\text{N}_4/\text{NiCoP}$ indicate uniformly dispersed regular spherical NiCoP nanoparticles with an average size of approximately 45 nm, which

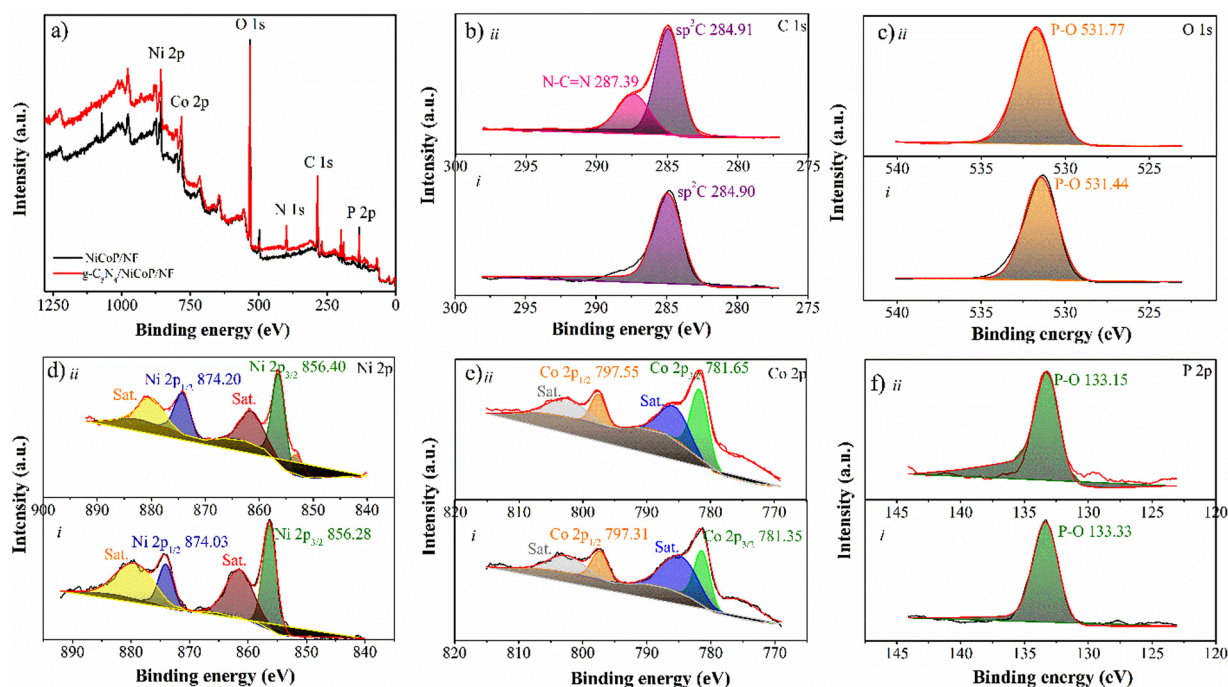


Fig. 2 XPS analyses of NiCoP/NF and $\text{g-C}_3\text{N}_4/\text{NiCoP}/\text{NF}$ electrodes: (a) survey spectrum and the high-resolution (b) C 1s, (c) O 1s, (d) Ni 2p, (e) Co 2p, and (f) P 2p.

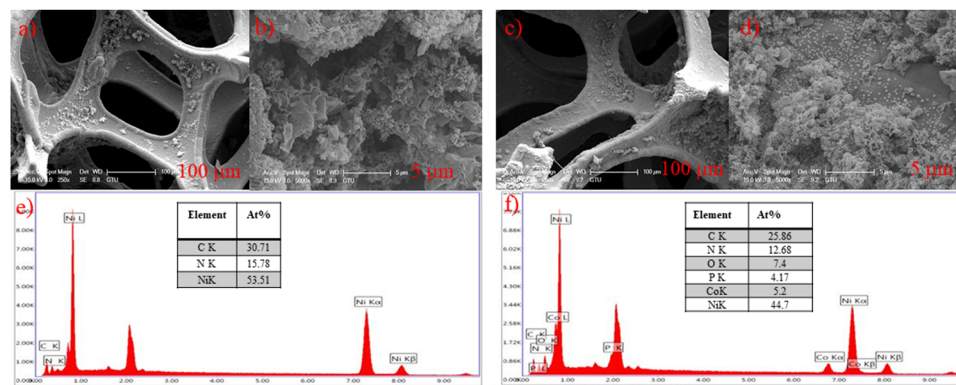


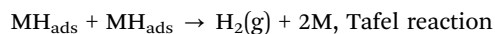
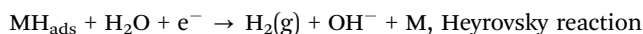
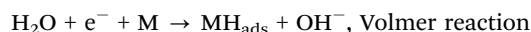
Fig. 3 Low- and high-resolution SEM images of (a) and (b) $g\text{-C}_3\text{N}_4/\text{NF}$, (c) and (d) $g\text{-C}_3\text{N}_4/\text{NiCoP}/\text{NF}$. EDS analysis of (e) $g\text{-C}_3\text{N}_4/\text{NF}$ and (f) $g\text{-C}_3\text{N}_4/\text{NiCoP}/\text{NF}$.

can be attributed to the controlled electrodeposition and $g\text{-C}_3\text{N}_4$ nanosheets (Fig. 3c and d). These results are consistent with the literature.⁴¹ The EDS analysis is presented in Fig. 3e and f, confirming the simultaneous presence of C, N, Ni, Co, and P.

3.3 Evaluation of the HER results

Electrocatalytic activity tests of $g\text{-C}_3\text{N}_4$ and $g\text{-C}_3\text{N}_4/\text{NiCoP}$ were performed in a three-electrode system in a 1.0 M KOH electrolyte. The electrocatalytic HER performances of the $g\text{-C}_3\text{N}_4$, NiCoP, $g\text{-C}_3\text{N}_4/\text{NiCoP}$, and Pt/C catalysts are recorded at a scanning speed of 2 mV s^{-1} by LSV, as shown in Fig. 4. It is known that a low overpotential is a very important parameter in determining the activity of a catalyst.⁵⁰ The commercial Pt/C catalyst exhibited an overpotential of 80 mV at a current density of 10 mA cm^{-2} with iR correction (50%) (Fig. 4a). The iR correction was developed to correct the voltage loss caused by the electrolyte solution between the working and the reference electrodes, where R is electrolyte solution resistance.⁵¹ The $g\text{-C}_3\text{N}_4/\text{NiCoP}$ catalyst exhibited an overpotential of 80 mV@ 10 mA cm^{-2} , similar to that of the Pt/C catalyst. The $g\text{-C}_3\text{N}_4/\text{NiCoP}$ catalyst exhibited a higher electrocatalytic activity than NiCoP and $g\text{-C}_3\text{N}_4$. When compared with the studies in the literature, the HER overpotential competes with those in the literature, as shown in Table S1 (ESI†). The Tafel slope can be found through the reaction mechanism and is often used to determine the HER and OER performance of the catalyst.⁵² Tafel plots were derived from the LSV curves to investigate the HER mechanism of the electrocatalysts (Fig. 4b). The Tafel slopes of $g\text{-C}_3\text{N}_4$, NiCoP, $g\text{-C}_3\text{N}_4/\text{NiCoP}$, and Pt/C were estimated as 121 mV dec^{-1} , 112 mV dec^{-1} , 96 mV dec^{-1} and 32 mV dec^{-1} , respectively. The Tafel slope of $g\text{-C}_3\text{N}_4/\text{NiCoP}$ indicates that the reaction occurs *via* the Volmer–Heyrovsky mechanism. Electrochemical desorption of H_2 is the rate-determining step in the kinetic process.⁵³ It has been reported that the Tafel step is the rate-determining step if the Tafel slope is below 30 mV , the Volmer step if the Tafel slope is above 120 mV dec^{-1} , and the Heyrovsky step if the slope is between $40\text{--}120\text{ mV dec}^{-1}$.⁵⁴ The Tafel slope of $g\text{-C}_3\text{N}_4/\text{NiCoP}$ is in the range of $40\text{--}120\text{ mV dec}^{-1}$, and the Heyrovsky step is the

rate-determining step. The Tafel slope of $g\text{-C}_3\text{N}_4/\text{NiCoP}$ is lower than those of the other electrocatalysts, indicating superior HER kinetics. The typical HER mechanism for the alkaline medium is as follows:⁵⁵



where M represents the metal active site and H_{ads} is the adsorbed H species. First, the adsorption of water onto the surface leads to the formation of a hydrogen atom adsorbed surface (MH_{ads}) and OH^- intermediate (Volmer reaction). Then, H_2 desorption from the surface occurs during the Heyrovsky or Tafel reactions.

The effect of $g\text{-C}_3\text{N}_4$ on HER activity was investigated, and the charge-transfer resistance (R_{ct}) of the catalysts was compared. The Nyquist plots of the catalysts are shown in Fig. 4c. The data fitted by the constant phase element (CPE) equivalent (inset of Fig. 4c) and estimated values are tabulated in Table S3 (ESI†). The $g\text{-C}_3\text{N}_4/\text{NiCoP}$ catalyst has a low R_{ct} value of $4.84\text{ k}\Omega$, while the $g\text{-C}_3\text{N}_4$ and NiCoP have a large R_{ct} of 7.29 and $5.16\text{ k}\Omega$, respectively. The small R_{ct} value indicates a faster electron transfer rate of the $g\text{-C}_3\text{N}_4/\text{NiCoP}$ catalyst than $g\text{-C}_3\text{N}_4$ and NiCoP, which contributes to enhancing the HER activity.^{56,57} The stability of the $g\text{-C}_3\text{N}_4/\text{NiCoP}$ catalyst was investigated for the HER in alkaline media by repeated 1000 LSV at 100 mV s^{-1} (Fig. 4d). The relative standard deviation (RSD) was estimated to be 27% at 10 mA cm^{-2} . Moreover, an amperometric current–time plot at a constant overpotential value (80 mV vs. RHE) was recorded for 15 h, as shown in Fig. S2a (ESI†). The catalyst showed an excellent HER stability. The SEM image and corresponding XRD pattern after the HER stability test are shown in Fig. S3 and S4 (ESI†), respectively. When the SEM images of the $g\text{-C}_3\text{N}_4/\text{NiCoP}$ catalyst before and after HER are compared, no significant difference is observed (Fig. S3a–c, ESI†). The XRD structural characterization also supports these conclusions (Fig. S4, ESI†).



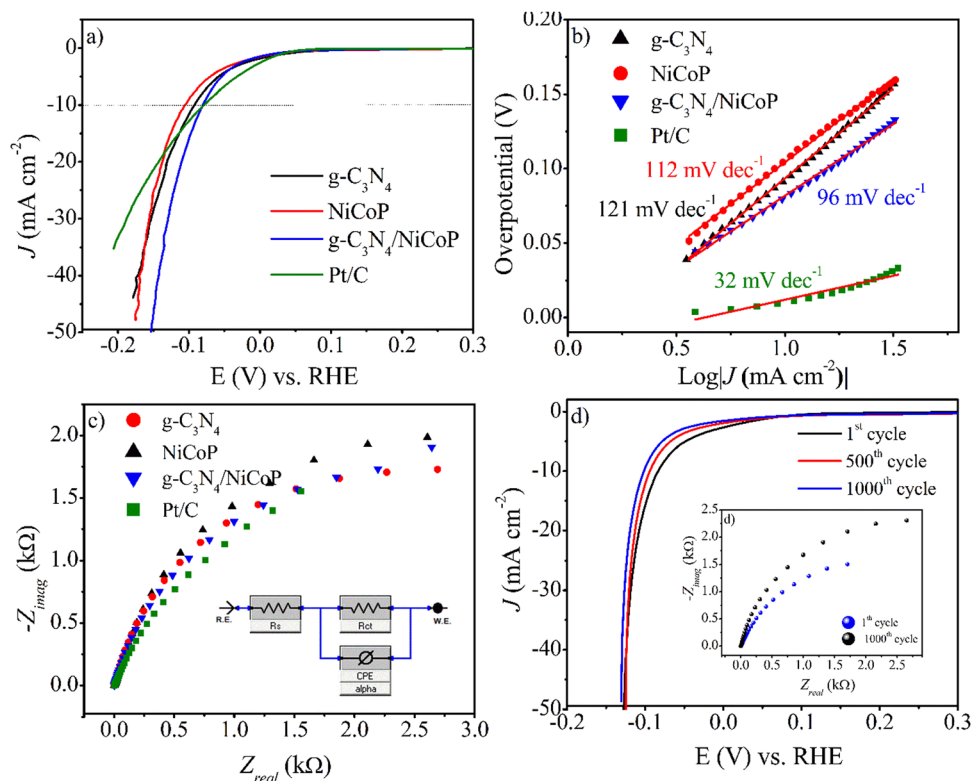
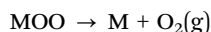
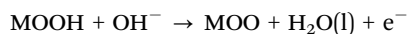
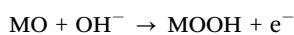
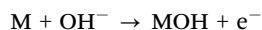


Fig. 4 LSVs of the catalysts of g-C₃N₄, NiCoP, g-C₃N₄/NiCoP, and Pt/C (a) (50% of *iR*-correction), (b) Tafel curves, and (c) EIS spectra. (d) LSVs of the g-C₃N₄/NiCoP for 1st, 500th, and 1000th cycles (inset: Nyquist plot of g-C₃N₄/NiCoP in initial and post-1000 cycles).

3.4 Evaluation of the OER results

The most probable mechanism for the OER in the alkaline electrolyte is as follows:⁵⁸



This mechanism is believed to occur in the presence of transition metal sites and phosphate catalysts, which are generally considered to be catalytically active centers.^{59,60} In the above equations, M represents a metal element with an active surface site. During this process, M reacts with the hydroxyl anions to form MOH. Then, MOH splits into a proton to form a water molecule and MO. MO recombines with hydroxyl anions to form MOOH. This process continues with MOO in the presence of hydroxyl anions, followed by the evolution of O₂.

The electrocatalytic activity of the g-C₃N₄/NiCoP catalyst in the OER was evaluated at a scan rate of 2 mV s⁻¹ in 1.0 M KOH using the LSV technique. As shown in Fig. 5a, the g-C₃N₄/NiCoP catalyst exhibits excellent OER performance, not only as a commercial RuO₂ catalyst, which is known to be the best

electrocatalyst for the OER with a low overpotential value at a current density of 10 mA cm⁻², but is also superior to NiCoP and g-C₃N₄. The g-C₃N₄/NiCoP catalyst only required an overpotential of 370 mV@10 mA cm⁻² with *iR* correction (50%). The catalytic current density of g-C₃N₄/NiCoP is 1.7 times higher than that of g-C₃N₄. The possibility of the formation of double Co–N and Ni–N bonds between g-C₃N₄ and NiCoP can facilitate charge transfer between Ni, Co, and P in the g-C₃N₄/NiCoP catalyst, triggering more active reaction sites and enhancing the electrocatalytic activity. The OER overpotential is moderate compared to that reported in the literature (Table S1, ESI†). The Tafel slopes of the catalysts are shown in Fig. 5b. The g-C₃N₄/NiCoP catalyst shows a Tafel slope of 64 mV dec⁻¹, whereas the g-C₃N₄ and NiCoP catalysts exhibit higher values of 65 and 70 mV dec⁻¹, respectively. This proves that g-C₃N₄ can lead to superior activity due to an increase in the reaction rate and kinetics. The Nyquist plots are shown in Fig. 5c. The g-C₃N₄/NiCoP catalyst exhibited a low *R*_{ct} according to g-C₃N₄ and NiCoP catalysts. Consecutive 1000 LSV measurements were performed at a scan rate of 100 mV s⁻¹ to determine the stability of the g-C₃N₄/NiCoP catalyst, as shown in Fig. 5d. Compared to the initial and post-1000 LSV cycles, there was no significant change in the current densities and onset potentials. This was also supported by the current–time plot at 370 mV of overpotential for 15 h (Fig. S2b, ESI†). The post-OER SEM images are similar to those of the pre-HER of the g-C₃N₄/NiCoP catalyst (Fig. S3a, b and d, ESI†). Post-OER XRD measurements support the stability of the catalyst



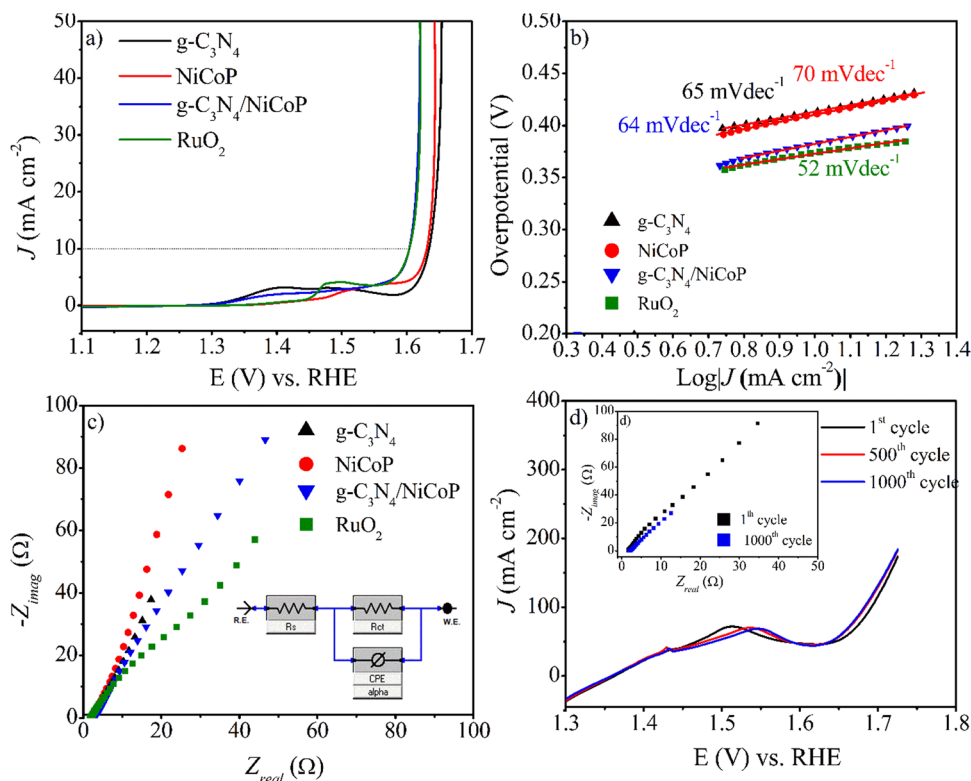


Fig. 5 The LSVs of catalysts of g-C₃N₄, NiCoP, g-C₃N₄/NiCoP, and RuO₂ (a) (50% of *iR*-correction), (b) Tafel curves, (c) EIS spectra. (d) LSVs of the g-C₃N₄/NiCoP for 1st, 500th, and 1000th cycles (inset: Nyquist plot of g-C₃N₄/NiCoP in initial and post-1000 cycles).

(Fig. S4, ESI†). These results were consistent with the EIS results (inset of Fig. 5d). Stability testing showed that this electrode was stable for a long time without any significant deviation.

The water electrolysis turnover frequency (TOF) of the electrocatalyst is an important activity parameter that reflects the HER or OER kinetics of the catalytic material.⁶¹ The TOF is calculated as follows^{61,62}:

$$\text{TOF} = j \times \frac{N_A}{n} \times F \times \Gamma$$

where *j* is the current density (A cm⁻²), *N_A* is the Avogadro number, *n* is the number of electrons (2 for H₂, 4 for O₂), *F* is the Faraday constant (96 485 C) and *Γ* is the surface

concentration of active sites. *Γ* is calculated from the recording of chronoamperograms at the same overpotential and the current-charge relationship. The TOF parameters of the catalysts are presented in detail in Table S4 (ESI†). The TOF values for the HER were calculated for g-C₃N₄/NiCoP/NF (0.029 s⁻¹), NiCoP/NF (0.027 s⁻¹) and g-C₃N₄/NF (0.027 s⁻¹) at the same overpotential. The TOF values of g-C₃N₄/NiCoP/NF, NiCoP/NF and g-C₃N₄/NF for the OER were calculated as 0.047 s⁻¹, 0.021 s⁻¹ and 0.022 s⁻¹, respectively. Remarkably, the TOF value of the g-C₃N₄/NiCoP/NF electrode was much higher than those of NiCoP/NF and g-C₃N₄/NF. These results show the superior intrinsic activity for the HER and OER of the g-C₃N₄/NiCoP electrocatalyst.

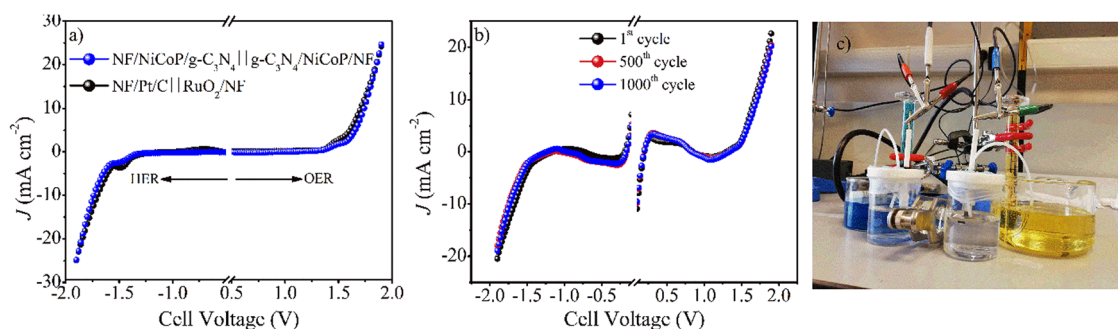


Fig. 6 (a) LSV curves of catalysts for overall water electrolysis, (b) electrochemical stability test on g-C₃N₄/NiCoP electrocatalysts, and (c) photograph of the alkaline water electrolysis system.



3.5 Evaluation of the overall water electrolysis results

Based on the HER and OER performance of the g-C₃N₄/NiCoP catalyst, the g-C₃N₄/NiCoP/NF electrode was used as both the anode and cathode material to determine the catalytic properties of this electrode in the OWE system (Fig. 6). The cell voltage of the NF/NiCoP/g-C₃N₄||g-C₃N₄/NiCoP/NF pair needs to be 1.70 V@10 mA cm⁻². This value is very close to the cell voltage (1.69 V@10 mA cm⁻²) of the NF/Pt/C||RuO₂/NF pair, which is used as a reference. The performance of the g-C₃N₄/NiCoP/NF electrolyzer was compared with that of the electrocatalysts containing NiCoP in the literature and it was found to be competitive, as shown in Table S1 (ESI†). Moreover, the electrochemical stability of the NF/NiCoP/g-C₃N₄||g-C₃N₄/NiCoP/NF electrolyzer was examined by LSV measurements for the initial and post-1000 cycles at 100 mV s⁻¹ (Fig. 6b). The photograph shows the used water electrolysis system, as shown in the inset of Fig. 6b. As a result, the NF/NiCoP/g-C₃N₄||g-C₃N₄/NiCoP/NF electrolyzer exhibited a low cell voltage and high stability for the OWE in alkaline media.

4. Conclusions

In summary, NiCoP is successfully synthesized by electrodeposition on the nickel foam. Then, the NiCoP/NF electrode is modified with g-C₃N₄ using a drop-dry process. g-C₃N₄ accelerates the charge-transfer process and enhances the electrocatalytic activity of the NiCoP catalyst. The g-C₃N₄/NiCoP/NF electrode exhibits excellent catalytic activity and stability toward both the HER and OER. The electrode requires a low overpotential of 80 mV and 370 mV at 10 mA cm⁻² for the HER and OER, respectively. The g-C₃N₄/NiCoP/NF electrode is employed as the cathode and anode in an alkaline water electrolyzer. It requires a cell voltage of 1.70 V to achieve a current density of 10 mA cm⁻². Moreover, the water electrolyzer exhibits a good long-term electrochemical stability. The g-C₃N₄/NiCoP/NF electrode can be used as an efficient electrocatalyst for overall water electrolysis because of its both low overpotential and high current density.

Conflicts of interest

There are no conflicts to declare.

References

- W. Zhai, Y. Ma, D. Chen, J. C. Ho, Z. Dai and Y. Qu, Recent progress on the long-term stability of hydrogen evolution reaction electrocatalysts, *InfoMat*, 2022, **4**, e12357, DOI: [10.1002/INF2.12357](#).
- S. Keshipour and A. Asghari, A review on hydrogen generation by phthalocyanines, *Int. J. Hydrogen Energy*, 2022, **47**, 12865–12881, DOI: [10.1016/j.ijhydene.2022.02.058](#).
- I. Dincer and C. Acar, Review and evaluation of hydrogen production methods for better sustainability, *Int. J. Hydrogen Energy*, 2015, **40**, 11094–11111, DOI: [10.1016/j.ijhydene.2014.12.035](#).
- P. C. K. Vesborg, B. Seger and I. Chorkendorff, Recent development in hydrogen evolution reaction catalysts and their practical implementation, *J. Phys. Chem. Lett.*, 2015, **6**, 951–957, DOI: [10.1021/ACS.JPCLETT.5B00306/SUPPL_FILE/JZ5B00306_SI_001.PDF](#).
- G. Gupta, D. Choudhury, R. Maurya, S. Sharma and M. Neergat, Investigation of Hydrogen Oxidation/Evolution Reactions Based on Charge-Transfer Coefficients Derived from Butler-Volmer and Eyring Analyses, *J. Phys. Chem. C*, 2023, **127**, 23566–23576, DOI: [10.1021/ACS.JPCC.3C05416/ASSET/IMAGES/LARGE/JP3C05416_0009.JPEG](#).
- D. Choudhury, R. Das, A. K. Tripathi, D. Priyadarshani and M. Neergat, Kinetics of Hydrogen Evolution Reactions in Acidic Media on Pt, Pd, and MoS₂, *Langmuir*, 2022, **38**, 4341–4350, DOI: [10.1021/ACS.LANGMUIR.2C00090/ASSET/IMAGES/LARGE/LA2C00090_0008.JPEG](#).
- Q. Chen, Y. Yu, J. Li, H. Nan, S. Luo, C. Jia, P. Deng, S. Zhong and X. Tian, Recent Progress in Layered Double Hydroxide-Based Electrocatalyst for Hydrogen Evolution Reaction, *ChemElectroChem*, 2022, **9**, e202101387, DOI: [10.1002/CELC.202101387](#).
- D. Choudhury, R. Das, R. Maurya, H. Kumawat and M. Neergat, Kinetics of the Oxygen Evolution Reaction (OER) on Amorphous and Crystalline Iridium Oxide Surfaces in Acidic Medium, *Langmuir*, 2023, **39**, 13748–13757, DOI: [10.1021/ACS.LANGMUIR.3C02293/ASSET/IMAGES/LARGE/LA3C02293_0007.JPEG](#).
- A. Ursúa, L. M. Gandía and P. Sanchis, Hydrogen production from water electrolysis: Current status and future trends, *Proc. IEEE*, 2012, **100**, 410–426, DOI: [10.1109/JPROC.2011.2156750](#).
- B. Chai, T. Peng, J. Mao, K. Li and L. Zan, Graphitic carbon nitride (g-C₃N₄)-Pt-TiO₂ nanocomposite as an efficient photocatalyst for hydrogen production under visible light irradiation, *Phys. Chem. Chem. Phys.*, 2012, **14**, 16745–16752, DOI: [10.1039/C2CP42484C](#).
- J. E. Park, S. Y. Kang, S. H. Oh, J. K. Kim, M. S. Lim, C. Y. Ahn, Y. H. Cho and Y. E. Sung, High-performance anion-exchange membrane water electrolysis, *Electrochim. Acta*, 2019, **295**, 99–106, DOI: [10.1016/j.electacta.2018.10.143](#).
- B. Buccheri, F. Ganci, B. Patella, G. Aiello, P. Mandin and R. Inguanta, Ni-Fe alloy nanostructured electrodes for water splitting in alkaline electrolyser, *Electrochim. Acta*, 2021, **388**, 138588, DOI: [10.1016/j.electacta.2021.138588](#).
- S. Anantharaj, H. Sugime and S. Noda, Surface amorphized nickel hydroxy sulphide for efficient hydrogen evolution reaction in alkaline medium, *Chem. Eng. J.*, 2021, **408**, 127275, DOI: [10.1016/j.cej.2020.127275](#).
- P. Arunkumar, S. Gayathri and J. H. Han, A Complementary Co-Ni Phosphide/Bimetallic Alloy-Interspersed N-Doped Graphene Electrocatalyst for Overall Alkaline Water Splitting, *ChemSusChem*, 2021, **14**, 1921–1935, DOI: [10.1002/CSSC.202100116](#).
- S. R. Kadam, S. Ghosh, R. Bar-Ziv and M. Bar-Sadan, Facile synthetic approach to produce optimized molybdenum



- carbide catalyst for alkaline HER, *Appl. Surf. Sci.*, 2021, **559**, 149932, DOI: [10.1016/j.apsusc.2021.149932](https://doi.org/10.1016/j.apsusc.2021.149932).
- 16 M. Abedini Mohammadi, M. Saghafi Yazdi, M. Talafi Noghani, A. Moghanian and S. A. Hosseini, Synthesis and optimization of Mo–Ni–Se@NiSe core-shell nanostructures as efficient and durable electrocatalyst for hydrogen evolution reaction in alkaline media, *Int. J. Hydrogen Energy*, 2022, **47**, 34455–34470, DOI: [10.1016/j.ijhydene.2022.08.025](https://doi.org/10.1016/j.ijhydene.2022.08.025).
 - 17 Z. Liu, J. Wang, C. Zhan, J. Yu, Y. Cao, J. Tu and C. Shi, Phosphide-oxide honeycomb-like heterostructure CoP@CoMoO₄/CC for enhanced hydrogen evolution reaction in alkaline solution, *J. Mater. Sci. Technol.*, 2020, **46**, 177–184, DOI: [10.1016/j.jmst.2019.12.013](https://doi.org/10.1016/j.jmst.2019.12.013).
 - 18 L. Chen, Y. Song, Y. Liu, L. Xu, J. Qin, Y. Lei and Y. Tang, NiCoP nanoleaves array for electrocatalytic alkaline H₂ evolution and overall water splitting, *J. Energy Chem.*, 2020, **50**, 395–401, DOI: [10.1016/j.jechem.2020.03.046](https://doi.org/10.1016/j.jechem.2020.03.046).
 - 19 F. Diao, W. Huang, G. Ctistis, H. Wackerbarth, Y. Yang, P. Si, J. Zhang, X. Xiao and C. Engelbrekt, Bifunctional and Self-Supported NiFeP-Layer-Coated NiP Rods for Electrochemical Water Splitting in Alkaline Solution, *ACS Appl. Mater. Interfaces*, 2021, **13**, 23702–23713, DOI: [10.1021/acsami.1c03089](https://doi.org/10.1021/acsami.1c03089)/ASSET/IMAGES/MEDIUM/AM1C03089_M007.GIF.
 - 20 Z. Guo, L. Liu, J. Wang, Y. Cao, J. Tu, X. Zhang and L. Ding, Recent progress in CoP-based materials for electrochemical water splitting, *Int. J. Hydrogen Energy*, 2021, **46**, 34194–34215, DOI: [10.1016/j.ijhydene.2021.07.236](https://doi.org/10.1016/j.ijhydene.2021.07.236).
 - 21 D. Chen, R. Lu, Z. Pu, J. Zhu, H. W. Li, F. Liu, S. Hu, X. Luo, J. Wu, Y. Zhao and S. Mu, Ru-doped 3D flower-like bimetallic phosphide with a climbing effect on overall water splitting, *Appl. Catal., B*, 2020, **279**, 119396, DOI: [10.1016/j.apcatb.2020.119396](https://doi.org/10.1016/j.apcatb.2020.119396).
 - 22 R. Zhang, X. Wang, S. Yu, T. Wen, X. Zhu, F. Yang, X. Sun, X. Wang, W. Hu, R. Zhang, X. Wang, S. Yu, T. Wen, X. Zhu, X. Sun, F. Yang and W. Hu, Ternary NiCo₂Px Nanowires as pH-Universal Electrocatalysts for Highly Efficient Hydrogen Evolution Reaction, *Adv. Mater.*, 2017, **29**, 1605502, DOI: [10.1002/adma.201605502](https://doi.org/10.1002/adma.201605502).
 - 23 L. Yu, I. K. Mishra, Y. Xie, H. Zhou, J. Sun, J. Zhou, Y. Ni, D. Luo, F. Yu, Y. Yu, S. Chen and Z. Ren, Ternary Ni_{2(1-x)}Mo_{2x}P nanowire arrays toward efficient and stable hydrogen evolution electrocatalysis under large-current-density, *Nano Energy*, 2018, **53**, 492–500, DOI: [10.1016/j.nanoen.2018.08.025](https://doi.org/10.1016/j.nanoen.2018.08.025).
 - 24 Y. Lian, H. Sun, X. Wang, P. Qi, Q. Mu, Y. Chen, J. Ye, X. Zhao, Z. Deng and Y. Peng, Carved nanoframes of cobalt-iron bimetal phosphide as a bifunctional electrocatalyst for efficient overall water splitting, *Chem. Sci.*, 2019, **10**, 464–474, DOI: [10.1039/C8SC03877E](https://doi.org/10.1039/C8SC03877E).
 - 25 H. Liang, A. N. Gandi, D. H. Anjum, X. Wang, U. Schwingenschlögl and H. N. Alshareef, Plasma-Assisted Synthesis of NiCoP for Efficient Overall Water Splitting, *Nano Lett.*, 2016, **16**, 7718–7725, DOI: [10.1021/acs.nanolett.6b03803](https://doi.org/10.1021/acs.nanolett.6b03803)/ASSET/IMAGES/LARGE/NL-2016-038036_0007.JPEG.
 - 26 J. L. Bian, Z. Y. Song, Y. Z. Zhang and C. W. Cheng, NiCoP nanopeapods embedded in carbon nanotube arrays as bifunctional catalysts for efficient overall water splitting, *Mater. Today Nano*, 2019, **8**, 100053, DOI: [10.1016/j.mtnano.2019.100053](https://doi.org/10.1016/j.mtnano.2019.100053).
 - 27 D. Akyüz, R. M. Zunain Ayaz, S. Yılmaz, Ö. Uğuz, C. Sarıoğlu, F. Karaca, A. R. Özkaya and A. Koca, Metal chalcogenide based photocatalysts decorated with heteroatom doped reduced graphene oxide for photocatalytic and photoelectrochemical hydrogen production, *Int. J. Hydrogen Energy*, 2019, **44**, 18836–18847, DOI: [10.1016/j.ijhydene.2019.04.049](https://doi.org/10.1016/j.ijhydene.2019.04.049).
 - 28 D. Akyüz, B. Keskin, U. Şahintürk and A. Koca, Electrocatalytic hydrogen evolution reaction on reduced graphene oxide electrode decorated with cobaltphthalocyanine, *Appl. Catal., B*, 2016, **188**, 217–226, DOI: [10.1016/j.apcatb.2016.02.003](https://doi.org/10.1016/j.apcatb.2016.02.003).
 - 29 H. Yu, L. Shang, T. Bian, R. Shi, G. I. N. Waterhouse, Y. Zhao, C. Zhou, L.-Z. Wu, C.-H. Tung, T. Zhang, H. Yu, L. Shang, T. Bian, R. Shi, Y. Zhao, C. Zhou, L. Wu, C. Tung, T. Zhang and G. I. N. Waterhouse, Nitrogen-Doped Porous Carbon Nanosheets Templated from g-C₃N₄ as Metal-Free Electrocatalysts for Efficient Oxygen Reduction Reaction, *Adv. Mater.*, 2016, **28**, 5080–5086, DOI: [10.1002/adma.201600398](https://doi.org/10.1002/adma.201600398).
 - 30 Z. W. Seh, K. D. Fredrickson, B. Anasori, J. Kibsgaard, A. L. Strickler, M. R. Lukatskaya, Y. Gogotsi, T. F. Jaramillo and A. Vojvodic, Two-Dimensional Molybdenum Carbide (MXene) as an Efficient Electrocatalyst for Hydrogen Evolution, *ACS Energy Lett.*, 2016, **1**, 589–594, DOI: [10.1021/acseenergylett.6b00247](https://doi.org/10.1021/acseenergylett.6b00247)/ASSET/IMAGES/LARGE/NZ-2016-002479_0005.JPEG.
 - 31 N. Tian, H. Huang, X. Du, F. Dong and Y. Zhang, Rational nanostructure design of graphitic carbon nitride for photocatalytic applications, *J. Mater. Chem. A*, 2019, **7**, 11584–11612, DOI: [10.1039/C9TA01819K](https://doi.org/10.1039/C9TA01819K).
 - 32 H. Jin, X. Liu, Y. Jiao, A. Vasileff, Y. Zheng and S. Z. Qiao, Constructing tunable dual active sites on two-dimensional C₃N₄@MoN hybrid for electrocatalytic hydrogen evolution, *Nano Energy*, 2018, **53**, 690–697, DOI: [10.1016/j.nanoen.2018.09.046](https://doi.org/10.1016/j.nanoen.2018.09.046).
 - 33 X. Wang, K. Maeda, A. Thomas, K. Takanabe, G. Xin, J. M. Carlsson, K. Domen and M. Antonietti, A metal-free polymeric photocatalyst for hydrogen production from water under visible light, *Nat. Mater.*, 2009, **8**(1), 76–80, DOI: [10.1038/nmat2317](https://doi.org/10.1038/nmat2317).
 - 34 H. Yu, P. Xiao, P. Wang and J. Yu, Amorphous molybdenum sulfide as highly efficient electron-cocatalyst for enhanced photocatalytic H₂ evolution, *Appl. Catal., B*, 2016, **193**, 217–225, DOI: [10.1016/j.apcatb.2016.04.028](https://doi.org/10.1016/j.apcatb.2016.04.028).
 - 35 Y. Wang, L. Liu, T. Ma, Y. Zhang, H. Huang, Y. H. Wang, L. Z. Liu, Y. H. Zhang, H. W. Huang and T. Y. Ma, 2D Graphitic Carbon Nitride for Energy Conversion and Storage, *Adv. Funct. Mater.*, 2021, **31**, 2102540, DOI: [10.1002/adfm.202102540](https://doi.org/10.1002/adfm.202102540).
 - 36 J. Liu, T. Zhang, Z. Wang, G. Dawson and W. Chen, Simple pyrolysis of urea into graphitic carbon nitride with recyclable adsorption and photocatalytic activity, *J. Mater. Chem.*, 2011, **21**, 14398–14401, DOI: [10.1039/C1JM12620B](https://doi.org/10.1039/C1JM12620B).



- 37 Y. Cao, Z. Chen, F. Ye, Y. Yang, K. Wang, Z. Wang, L. Yin and C. Xu, One-step synthesis of amorphous NiCoP nanoparticles by electrodeposition as highly efficient electrocatalyst for hydrogen evolution reaction in alkaline solution, *J. Alloys Compd.*, 2022, **896**, 163103, DOI: [10.1016/J.JALLCOM.2021.163103](https://doi.org/10.1016/J.JALLCOM.2021.163103).
- 38 K. Anuratha, Y. Su, M. Huang, C. Hsieh, Y. Xiao and J. Lin, High-performance hybrid supercapacitors based on electrodeposited amorphous bimetallic nickel cobalt phosphide nanosheets, *J. Alloys Compd.*, 2022, **897**, 163031, DOI: [10.1016/j.jallcom.2021.163031](https://doi.org/10.1016/j.jallcom.2021.163031).
- 39 X. Xia, B. Xu, H. Zhang, K. Ji, X. Ji, D. Wang and P. Yang, NiCoP/g-C₃N₄ Schottky heterojunctions towards efficient photocatalytic NO oxidation, *J. Alloys Compd.*, 2022, **928**, 167207, DOI: [10.1016/J.JALLCOM.2022.167207](https://doi.org/10.1016/J.JALLCOM.2022.167207).
- 40 H. Yan and H. Yang, TiO₂-g-C₃N₄ composite materials for photocatalytic H₂ evolution under visible light irradiation, *J. Alloys Compd.*, 2011, **509**, L26-L29, DOI: [10.1016/J.JALLCOM.2010.09.201](https://doi.org/10.1016/J.JALLCOM.2010.09.201).
- 41 C. Jin, C. Xu, W. Chang, X. Ma, X. Hu, E. Liu and J. Fan, Bimetallic phosphide NiCoP anchored g-C₃N₄ nanosheets for efficient photocatalytic H₂ evolution, *J. Alloys Compd.*, 2019, **803**, 205-215, DOI: [10.1016/J.JALLCOM.2019.06.252](https://doi.org/10.1016/J.JALLCOM.2019.06.252).
- 42 H. S. Hu, Y. Li, Y. R. Shao, K. X. Li, G. Deng, C. Bin Wang and Y. Y. Feng, NiCoP nanorod arrays as high-performance bifunctional electrocatalyst for overall water splitting at high current densities, *J. Power Sources*, 2021, **484**, 229269, DOI: [10.1016/J.JPOWSOUR.2020.229269](https://doi.org/10.1016/J.JPOWSOUR.2020.229269).
- 43 K. S. Anuratha, Y. Z. Su, M. K. Huang, C. K. Hsieh, Y. Xiao and J. Y. Lin, High-performance hybrid supercapacitors based on electrodeposited amorphous bimetallic nickel cobalt phosphide nanosheets, *J. Alloys Compd.*, 2022, **897**, 163031, DOI: [10.1016/J.JALLCOM.2021.163031](https://doi.org/10.1016/J.JALLCOM.2021.163031).
- 44 L. Bi, X. Gao, L. Zhang, D. Wang and X. Zou, T. Xie, Enhanced Photocatalytic Hydrogen Evolution of NiCoP/g-C₃N₄ with Improved Separation Efficiency and Charge Transfer Efficiency, *ChemSusChem*, 2018, **11**, 276-284, DOI: [10.1002/cssc.201701574](https://doi.org/10.1002/cssc.201701574).
- 45 Z. Wang, W. Xu, T. Ding and Q. Yang, Controlled Synthesis of NiCoP/g-C₃N₄ Heterostructured Hybrids for Enhanced Visible-Light-Driven Hydrogen Evolution, *ChemistrySelect*, 2021, **6**, 5967-5974, DOI: [10.1002/SLCT.202101304](https://doi.org/10.1002/SLCT.202101304).
- 46 M. Li, Y. Luo, C. Jia, Q. Zhang, G. Luo, L. Zhao, R. Boukherroub and Z. Jiang, Facile Synthesis of Bimetal Nickel Cobalt Phosphate Nanostructures for High-Performance Hybrid Supercapacitors, *J. Alloys Compd.*, 2022, **893**, 162340, DOI: [10.1016/J.JALLCOM.2021.162340](https://doi.org/10.1016/J.JALLCOM.2021.162340).
- 47 J. G. Wang, W. Hua, M. Li, H. Liu, M. Shao and B. Wei, Structurally Engineered Hyperbranched NiCoP Arrays with Superior Electrocatalytic Activities toward Highly Efficient Overall Water Splitting, *ACS Appl. Mater. Interfaces*, 2018, **10**, 41237-41245, DOI: [10.1021/ACSAMI.8B11576/ASSET/IMAGES/LARGE/AM-2018-115769_0005.JPEG](https://doi.org/10.1021/ACSAMI.8B11576/ASSET/IMAGES/LARGE/AM-2018-115769_0005.JPEG).
- 48 Y. Zhang, Q. Shao, S. Long and X. Huang, Cobalt-molybdenum nanosheet arrays as highly efficient and stable earth-abundant electrocatalysts for overall water splitting, *Nano Energy*, 2018, **45**, 448-455, DOI: [10.1016/J.NANOEN.2018.01.022](https://doi.org/10.1016/J.NANOEN.2018.01.022).
- 49 K. Zhan, C. Feng, X. Feng, D. Zhao, S. Yue, Y. Li, Q. Jiao, H. Li and Y. Zhao, Iron-Doped Nickel Cobalt Phosphide Nanoarrays with Urchin-like Structures as High-Performance Electrocatalysts for Oxygen Evolution Reaction, *ACS Sustainable Chem. Eng.*, 2020, **8**, 6273-6281, DOI: [10.1021/ACSSUSCHEMENG.9B07781](https://doi.org/10.1021/ACSSUSCHEMENG.9B07781).
- 50 J. K. Nørskov, J. Rossmeisl, A. Logadottir, L. Lindqvist, J. R. Kitchin, T. Bligaard and H. Jónsson, Origin of the overpotential for oxygen reduction at a fuel-cell cathode, *J. Phys. Chem. B*, 2004, **108**, 17886-17892, DOI: [10.1021/JP047349J/ASSET/IMAGES/LARGE/JP047349JF00008.JPEG](https://doi.org/10.1021/JP047349J/ASSET/IMAGES/LARGE/JP047349JF00008.JPEG).
- 51 W. Zheng, iR Compensation for Electrocatalysis Studies: Considerations and Recommendations, *ACS Energy Lett.*, 2023, **8**, 1952-1958, DOI: [10.1021/ACSENERGYLETT.3C00366/ASSET/IMAGES/LARGE/NZ3C00366_0005.JPEG](https://doi.org/10.1021/ACSENERGYLETT.3C00366/ASSET/IMAGES/LARGE/NZ3C00366_0005.JPEG).
- 52 J. Wang, W. Cui, Q. Liu, Z. Xing, A. M. Asiri, X. Sun, J. Wang, W. Cui, Q. Liu, Z. Xing, X. Sun and A. M. Asiri, Recent progress in cobalt-based heterogeneous catalysts for electrochemical water splitting, *Adv. Mater.*, 2015, **28**, 215-230, DOI: [10.1002/adma.201502696](https://doi.org/10.1002/adma.201502696).
- 53 H. Zhu, Q. Li, H. Zhang, J. Liu, J. Li, Z. Zou, T. Hu and C. M. Li, Directly Grow Ultrasmall Co₂P QDs on MoS₂ Nanosheets to Form Heterojunctions Greatly Boosting Electron Transfer toward Hydrogen Evolution, *J. Phys. Chem. C*, 2023, **127**, 9681-9689, DOI: [10.1021/ACS.JPCC.3C01481/ASSET/IMAGES/LARGE/JP3C01481_0007.JPEG](https://doi.org/10.1021/ACS.JPCC.3C01481/ASSET/IMAGES/LARGE/JP3C01481_0007.JPEG).
- 54 M. A. Bhat and K. Majid, Metal-Organic Framework-Derived FeCo₂S₄/Co₃O₄ Heterostructure with Enhanced Electrocatalytic Performance for Oxygen Evolution and Hydrogen Evolution Reactions, *Langmuir*, 2023, **39**, 8224-8233, DOI: [10.1021/ACS.LANGMUIR.3C00695/ASSET/IMAGES/LARGE/LA3C00695_0008.JPEG](https://doi.org/10.1021/ACS.LANGMUIR.3C00695/ASSET/IMAGES/LARGE/LA3C00695_0008.JPEG).
- 55 S. Wang, Y. Song, Y. Sun, G. Guan, Q. Wang, Y. Shang, F. Guo, J. Xu, R. Pang and Y. Zhang, Rational Assembly of the NiMoP/NiCoZn Heterostructure Electrocatalyst for the Hydrogen Evolution Reaction at High Current Densities, *J. Phys. Chem. C*, 2023, **127**, 958-967, DOI: [10.1021/ACS.JPCC.2C07516/ASSET/IMAGES/LARGE/JP2C07516_0007.JPEG](https://doi.org/10.1021/ACS.JPCC.2C07516/ASSET/IMAGES/LARGE/JP2C07516_0007.JPEG).
- 56 S. Xu, M. Wang, G. Saranya, N. Chen, L. Zhang, Y. He, L. Wu, Y. Gong, Z. Yao, G. Wang, Z. Wang, S. Zhao, H. Tang, M. Chen and H. Gou, Pressure-driven catalyst synthesis of Co-doped Fe₃C@Carbon nano-onions for efficient oxygen evolution reaction, *Appl. Catal., B*, 2020, **268**, 118385, DOI: [10.1016/J.APCATB.2019.118385](https://doi.org/10.1016/J.APCATB.2019.118385).
- 57 G. Fang, J. Gao, J. Lv, H. Jia, H. Li, W. Liu, G. Xie, Z. Chen, Y. Huang, Q. Yuan, X. Liu, X. Lin, S. Sun and H. J. Qiu, Multi-component nanoporous alloy/(oxy)hydroxide for bifunctional oxygen electrocatalysis and rechargeable Zn-air batteries, *Appl. Catal., B*, 2020, **268**, 118431, DOI: [10.1016/J.APCATB.2019.118431](https://doi.org/10.1016/J.APCATB.2019.118431).
- 58 Y. Yan, B. Y. Xia, B. Zhao and X. Wang, A review on noble-metal-free bifunctional heterogeneous catalysts for overall electrochemical water splitting, *J. Mater. Chem. A*, 2016, **4**, 17587-17603, DOI: [10.1039/C6TA08075H](https://doi.org/10.1039/C6TA08075H).
- 59 J. Li, G. Wei, Y. Zhu, Y. Xi, X. Pan, Y. Ji, I. V. Zatovsky and W. Han, Hierarchical NiCoP nanocone arrays supported on



- Ni foam as an efficient and stable bifunctional electrocatalyst for overall water splitting, *J. Mater. Chem. A*, 2017, **5**, 14828–14837, DOI: [10.1039/C7TA03947F](https://doi.org/10.1039/C7TA03947F).
- 60 H. Kim, J. Park, I. Park, K. Jin, S. E. Jerng, S. H. Kim, K. T. Nam and K. Kang, Coordination tuning of cobalt phosphates towards efficient water oxidation catalyst, *Nat. Commun.*, 2015, **6**(1), 1–11, DOI: [10.1038/ncomms9253](https://doi.org/10.1038/ncomms9253).
- 61 S. Anantharaj, S. R. Ede, K. Karthick, S. Sam Sankar, K. Sangeetha, P. E. Karthik and S. Kundu, Precision and correctness in the evaluation of electrocatalytic water splitting: revisiting activity parameters with a critical assessment, *Energy Environ. Sci.*, 2018, **11**, 744–771, DOI: [10.1039/C7EE03457A](https://doi.org/10.1039/C7EE03457A).
- 62 S. Anantharaj, P. E. Karthik and S. Kundu, Self-assembled IrO₂ nanoparticles on a DNA scaffold with enhanced catalytic and oxygen evolution reaction (OER) activities, *J. Mater. Chem. A*, 2015, **3**, 24463–24478, DOI: [10.1039/C5TA07075A](https://doi.org/10.1039/C5TA07075A).

